

Your Interlibrary Loan request has been sent by email in a PDF format.

If this PDF arrives with an incorrect OCLC status, please contact lending located below.

#### Concerning Copyright Restrictions

The copyright law of the United States (Title 17, United States Code) governs the making of photocopies or other reproductions of copyrighted materials. Under certain conditions specified in the law, libraries and archives are authorized to furnish a photocopy or other reproduction. One of these specified conditions is that the photocopy or reproduction is not to be "used for any purpose other than private study, scholarship, or research". If a user makes a request for, or later uses, a photocopy or reproduction for purpose in excess of "fair use", that user may be liable for copyright infringement. This institution reserves the right to refuse to accept a copying order if, in its judgment, fulfillment of the order would involve violation of copyright law.

: GI : : UW`hmUbX`GHUZZ`D`YUgY`fYZYf`hc`7cdmf][ \hFYgci fWg`FYgYUfW` ; i ]XY`Zcf`  
UXX]h]cbU`]bZcfa Uh]cb `Uh`\hd.##[ i ]XYg""]V"Zgi "YXi #Wdmf][ \h

Interlibrary Loan Services: We Search the World for You...and Deliver!

Interlibrary Loan Services – FSU Community  
James Elliott – Resource Sharing Manager  
The Florida State University  
R.M. Strozier Library  
116 Honors Way  
Tallahassee, Florida 32306-2047  
Email: lib-borrowing@fsu.edu  
Website: <https://www.lib.fsu.edu/service/interlibrary-loan>  
Phone: 850.644.4466

#### **Non-FSU Institutions:**

Lib-Lending@fsu.edu  
850.644.4171

# Rapid #: -15736245

CROSS REF ID: **987688**

LENDER: **TMA :: Ejournals**

BORROWER: **FDA :: Main Library**

TYPE: Article CC:CCG

JOURNAL TITLE: Journal of fluids engineering

USER JOURNAL TITLE: Journal of Fluids Engineering

ARTICLE TITLE: Natural Convection Heat Transfer of Non-Newtonian Power-Law Fluids Within an Array of Elliptic Cylinders

ARTICLE AUTHOR:

VOLUME: 142

ISSUE: 1

MONTH:

YEAR: 2020

PAGES: 011105 (12 pages)

ISSN: 0098-2202

OCLC #:

Processed by RapidX: 2/5/2020 2:51:34 PM



This material may be protected by copyright law (Title 17 U.S. Code)

# Natural Convection Heat Transfer of Non-Newtonian Power-Law Fluids Within an Array of Elliptic Cylinders

**A. Torkfar**

Department of Mechanical Engineering,  
Amirkabir University of Technology,  
Tehran 1591634311, Iran  
e-mail: Arman.Torkfar@aut.ac.ir

**S. M. A. Noori Rahim Abadi<sup>1</sup>**

Department of Engineering Sciences,  
University West,  
Trollhättan 46135, Sweden  
e-mail: ali.abadi@hv.se

**A. Ahmadpour**

Department of Mechanical Engineering,  
Amirkabir University of Technology,  
Tehran 1591634311, Iran  
e-mail: Ali.ahmadpour@aut.ac.ir

*In this study, natural convection of non-Newtonian power-law fluids around an array of elliptic cylinders has been investigated numerically. The governing equations have been solved using an in-house computational fluid dynamics code based on the well-known finite volume method. It is assumed that the flow and temperature fields are laminar, steady, and two-dimensional. Furthermore, due to the low-temperature difference between the tube walls and the surrounding fluid, the changes in the physical properties of the fluids are neglected. The numerical results are validated against the available experimental and numerical results. The results show that by increasing the non-Newtonian fluid power-law index, the ratio of average Nusselt number of the  $i$ th cylinder to the average Nusselt number of a single cylinder under identical thermal conditions decreases. Moreover, it is found that the increase in the ratio of the distance between elliptic centers and the elliptic vertical diameter increases the ratio of the average Nusselt number of  $i$ th cylinder to the average Nusselt number for a single cylinder. Finally, a mathematical expression is given for the array averaged Nusselt number.*  
 [DOI: 10.1115/1.4044630]

**Keywords:** natural convection, non-Newtonian fluid, elliptic cylinders, power-law index

## 1 Introduction

Natural convection heat transfer over tube arrays is one of the most important subjects in the thermal-fluid sciences. This phenomenon can be seen in many engineering applications such as desalination, power plants, and nuclear reactions [1–3]. In most cases, the tube array consists of cylindrical tubes, but there are some particular cases in which elliptic tubes are used [4–6]. The elliptic tube configurations in natural convection phenomenon showed better heat transfer performance in some cases [4]. Non-Newtonian fluids in the tube array configuration have received considerable interests due to their vast range of applications such as electronic chips cooling, polymer processes, and food industries [7,8]. Moreover, the thermal performance for shear thinning non-Newtonian fluid is superior compared to the Newtonian fluid.

There are many numerical [9–11] and experimental [12–14] studies on the natural convection phenomenon of non-Newtonian fluids in different geometries. Lemus-Mondaca et al. [15] investigated the conjugate natural convection phenomenon during the sterilization process of Newtonian and non-Newtonian liquids numerically. They found that when the power-law index was  $n = 0.6$  (means a shear thinning fluid), the sterilization process time decreased 25% compared to the case of  $n = 1$ .

Alsabery et al. [16] numerically studied the effect of nanoparticle concentration on the natural convection heat transfer of non-Newtonian fluid inside a cavity. They used the finite element method to solve the governing equations. They considered different parameters such as Rayleigh number, phase deviation, amplitude ratio, power-law index, sidewall inclination angle, nanoparticle volume fraction, and dimensionless time in their study. Their results showed that the heat transfer rate increased

significantly with the increases in sidewall inclination angle and phase deviation.

In another work, Moraga et al. [17] studied the conjugate transient natural convection of power-law fluid over a three-dimensional cube using an in-house code based on finite volume method. Their results were successfully applied to achieve the optimum power-law index for the non-Newtonian fluids used in the food processing industry.

Matin et al. [18] numerically investigated the natural convection of power-law fluid in a cubic annulus. They found that an increase of the power-law index from 0.6 to 1.4 resulted in a decrease in the average Nusselt number. Their results also showed a minimum value for the Nusselt number, which was dependent on the eccentricity of the annulus. It was also found that the Prandtl number has no considerable effect on the heat transfer coefficient.

Alloui and Vasseur [19] investigated the natural convection of Carreau–Yasuda non-Newtonian fluids in a cavity numerically. They derived a semi-analytical solution based on the parallel flow approximation. They found that the value of the average viscosity decreased with the increase in Ra number and the decrease in fluid index.

Laminar natural convection of Newtonian and Bingham fluids in cylindrical annular enclosures studied numerically by Yigit et al. [20]. They found that the strength of the buoyancy force increased with the increase in Rayleigh number for both Newtonian and Bingham fluids. It was also found that the mean Nusselt numbers for Bingham fluids were smaller than those for Newtonian fluids because of additional flow resistance arising from yield stress in Bingham fluids.

Kefayati [21] used the finite difference lattice Boltzmann method for the simulation of natural convection of non-Newtonian molten polymer in a cavity. He found that an increase in the power-law index led to a significant decrease in the heat transfer rate. He also investigated the effect of magnetic field on the natural convection heat transfer of non-Newtonian molten

<sup>1</sup>Corresponding author.

Contributed by the Fluids Engineering Division of ASME for publication in the JOURNAL OF FLUIDS ENGINEERING. Manuscript received May 4, 2019; final manuscript received August 2, 2019; published online October 4, 2019. Associate Editor: Sergio Pirozzoli.

polymer [22,23]. His results showed that the increase in magnetic field strength decreased the effect of the power-law index on heat transfer. Moreover, he found that increment of the power-law index in the absence of the magnetic field caused a decrease in heat transfer rate.

There are also many works on the natural convection of non-Newtonian fluids over cylinders [24–27]. As an example of such studies, Shyam et al. [28] studied the natural convection of power-law fluid over a circular cylinder numerically. They considered all nondimensional numbers that the numerical solution depended on including Grashof number, Prandtl number, power-law index, and relative positioning of the cylinder with reference to the bottom wall in their simulations. They found that the heat transfer coefficient increased with the increase in Grashof and Prandtl numbers, and distance between the cylinder and the bottom wall.

Tiwari and Chhabra [29] simulated the natural convection of power-law fluid over a semicylinder using ANSYS FLUENT commercial software package. Their results showed that the local Nusselt number became maximum at the sharp corner of the cylinder. They also found that the average Nusselt number increased with the increase in the Grashof and Prandtl numbers and the decrease in the power-law index.

Numerical study on the natural convection of non-Newtonian fluids over tube bundle has not received considerable attention so far. The works in this field were limited to the Newtonian fluids [4–6,30]. The literature review shows that there is no work on the natural convection of non-Newtonian power-law fluid over elliptic tube bundle. In a real application, natural convection heat transfer commonly occurs on the surface of a tube bundle, and the development of the thermal boundary layer around lower tubes significantly influences the heat transfer rates of upper tubes. Therefore, it is the purpose of this study to numerically investigate the effect of main parameters such as Grashof number, Prandtl number, tube to tube spacing (bundle effect), power-law index, and ellipse orientation on the heat transfer coefficient within an elliptic tube bundle. To reach this goal, the present manuscript is organized as follows: In Sec. 2, the governing equations and the adapted numerical method are presented then followed by Sec. 3, the presentation of our numerical results. Finally, the work is concluded by Sec. 4 stating the main findings.

## 2 Problem Statement

**2.1 Computational Domain.** In this study, the natural convection of non-Newtonian power-law fluids within an elliptic tube bundle has been numerically investigated. The computational domain as well as the utilized grid in this study, which consists of a five-cylinder vertical array, is shown in Fig. 1. The horizontal and vertical diameters of each elliptic cylinder are assumed to be  $2b$  and  $2a$ , respectively. Moreover, the center to center distance between each two consecutive cylinders is assumed to be uniform,  $S$ , and the total distance between the first and the fifth cylinder is  $H$ . The computational domain is spanned  $80a$  and  $12b$  in the vertical and horizontal directions, respectively, in order to eliminate the effect of boundary conditions on the thermal performance of cylinders. The parameter  $E$  is also defined as the ratio of the horizontal ellipse diameter to the vertical one ( $b/a$ ).

**2.2 Governing Equations.** The following assumptions have been made for presenting the governing equations of natural convection of power-law non-Newtonian fluids:

- (1) The flow field is steady, laminar, and two-dimensional.
- (2) As the temperature difference between cylinder walls and the quiescent fluid,  $\Delta T$ , is low, the thermophysical properties of the fluid are assumed to be constant [31,32].
- (3) The buoyancy effect is considered through the Boussinesq approximation.
- (4) The fluid is incompressible, and the effect of viscous dissipation is negligible.

Moreover, the nondimensional variables are defined as (stared variables are dimensional)

$$\begin{aligned} \mathbf{U} &= \frac{\mathbf{U}^*}{U_c} & X &= \frac{X^*}{2a} & P &= \frac{P^*}{\rho_\infty U_c^2} \\ \boldsymbol{\tau} &= \frac{\boldsymbol{\tau}^*}{m \left( \frac{U_c}{2a} \right)^n} & T &= \frac{(T^* - T_\infty)}{(T_w - T_\infty)} \end{aligned} \quad (1)$$

where  $\mathbf{U}$  and  $X$  are the velocity and position vectors, respectively, and  $P$  and  $T$  are fluid pressure and temperature, respectively. Furthermore,  $m$  is the consistency index,  $\boldsymbol{\tau}$  is stress tensor of power-law fluid,  $n$  is the power-law index, and  $T_w$  and  $T_\infty$  are the cylinders and quiescent temperatures, respectively. Finally,  $U_c$  is the velocity scale of the problem, and it is chosen as  $\sqrt{2ag\beta\Delta T}$  and  $\beta$  is the coefficient of volume expansion,  $\Delta T$  is the temperature difference between solid surfaces and the fluid, and  $g$  is the gravitational acceleration.

Base on the abovementioned assumptions and by using nondimensional variables presented in Eq. (1), the dimensionless governing equations in the present numerical simulations are presented as follows [31,32]:

- (1) Continuity equation

$$\frac{\partial U_i}{\partial X_i} = 0 \quad (2)$$

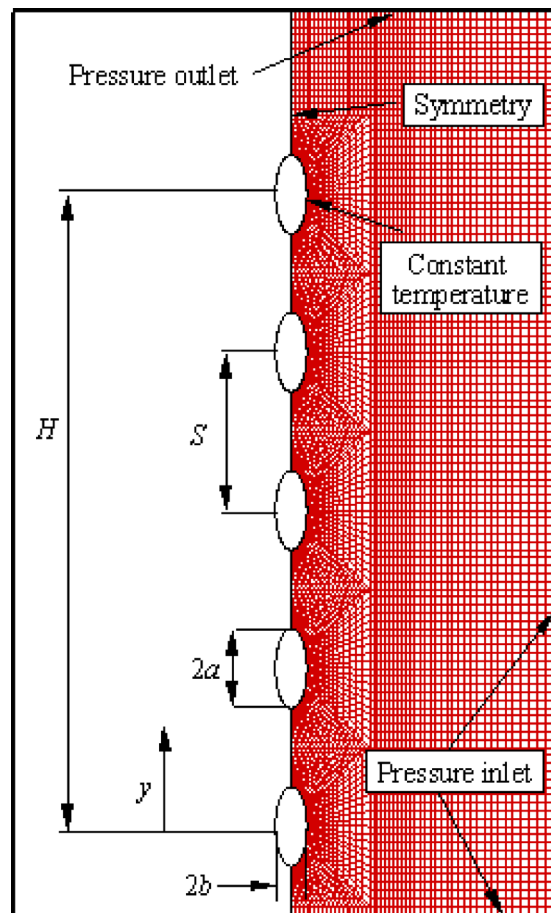


**Fig. 1 Computational domain, utilized grid, and relevant boundary conditions**

(2) Momentum equation

$$U_j \frac{\partial U_i}{\partial X_j} = - \frac{\partial P}{\partial X_i} + \frac{1}{\sqrt{\text{Gr}}} \left( \frac{\partial \tau_{ij}}{\partial X_j} \right) \quad (3)$$

(3) Energy equation

$$U_j \frac{\partial T}{\partial X_j} = \frac{1}{\text{Pr} \text{Gr}^{\frac{1}{n+1}}} \left( \frac{\partial^2 T}{\partial X_j \partial X_j} \right) \quad (4)$$

In the governing equations, Gr is the Grashof number and Pr is the Prandtl number. For a power-law fluid, the stress tensor  $\tau$  is also defined as [31,32]

$$\tau_{ij} = 2\eta e_{ij}$$

$$e_{ij} = \frac{1}{2} \left( \frac{\partial U_i}{\partial X_j} + \frac{\partial U_j}{\partial X_i} \right), \quad \eta = m \left( \frac{I_2}{2} \right)^{\frac{n-1}{2}}, \quad I_2 = \sum_i \sum_j e_{ij} e_{ij} \quad (5)$$

In this study, the definitions for the Gr, Pr, and Ra numbers of the non-Newtonian fluids are defined as [31,32]

$$\text{Gr} = \frac{\rho^2 (2a)^{n+2} (g\beta\Delta T)^{2-n}}{m^2} \quad (6)$$

$$\text{Pr} = \frac{\rho C}{k} \left( \frac{m}{\rho} \right)^{\frac{2}{1+n}} (2a)^{\frac{1-n}{1+n}} (2ag\beta\Delta T)^{\frac{3(n-1)}{2(n+1)}} \quad (7)$$

$$\text{Ra} = \text{Gr} \times \text{Pr} \quad (8)$$

where  $\rho$  is the density,  $k$  is the thermal conductivity,  $C$  is the specific heat capacity, and  $m$  is the power-law consistency index which controls the magnitude of the apparent viscosity for the power-law fluid and  $n$  is the power-law exponent which determines the slope of viscosity variation for the power-law model as it is shown in Fig. 2. Moreover, Grashof number is the ratio of buoyant force to viscous force, Prandtl number is the ratio of momentum to thermal diffusions, and Rayleigh number is the ratio of time scales for the thermal diffusion and the thermal convection.

**2.3 Numerical Method and Boundary Conditions.** In this study, an in-house computational fluid dynamics code based on

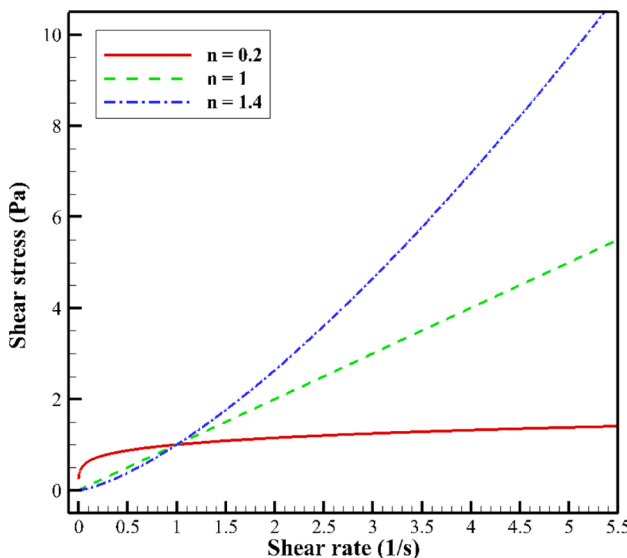
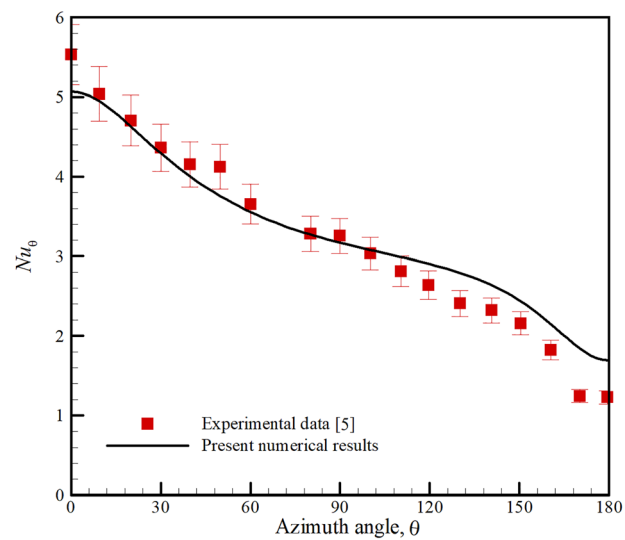


Fig. 2 The effect of power-law exponent on the shear stress-shear rate flow curve ( $m = 1$ )

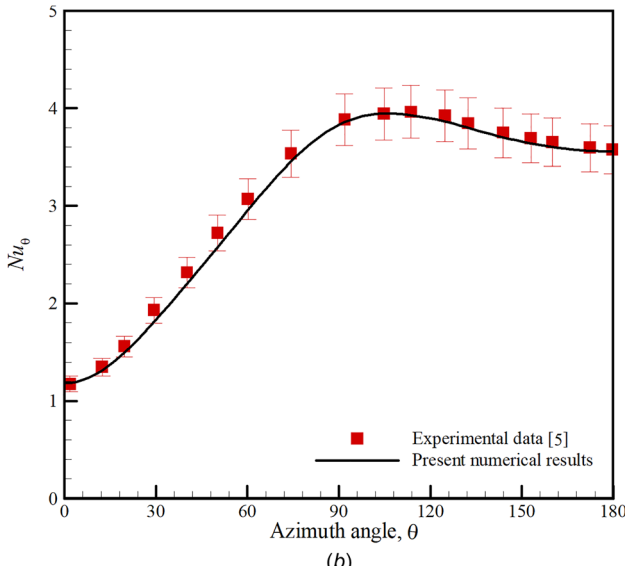
**Table 1 Specifications of the numerical cases**

Nondimensional numbers					
Gr	Pr	E	n	S/2a	Case number
2000	10	0.4	0.2, 1, 1.4	2	1
2000	10	2.5	0.2, 1, 1.4	2	2
2000	1, 10, 100	0.4	0.2, 1, 1.4	3	3
2000	1, 10, 100	2.5	0.2, 1, 1.4	3	4

the finite volume method is used to solve the system of coupled governing equations. The SIMPLE method is also employed to handle the pressure–velocity coupling [33]. A second-order upwind scheme approximates the convective terms in governing equations, while a second-order central differencing scheme discretizes the diffusive terms. Furthermore, the convergence criterion is set to  $10^{-5}$  for the residual of each parameter. The generalized minimal residual iterative method with a proper incomplete lower-upper preconditioner was used for solving the linear system of equations arising from finite volume



(a)



(b)

Fig. 3 Comparison between the present numerical results and the experimental data of Yusefi and Ashjaee [5] for a Newtonian fluid around a single ellipse at  $\text{Pr} = 0.7$  and  $\text{Ra} = 1000$ : (a)  $E = 0.67$  and (b)  $E = 1.25$

discretization of the governing equations. The multigrid method with a “V-cycle” was also utilized to improve the convergence rate of numerical simulations. The Gauss cell-based scheme approximated the gradient and central differencing was used for the Laplacian discretization.

The following boundary conditions are set for the numerical simulations:

- (1) Only half of the domain is simulated due to the symmetry of the cylinder array.
- (2) No-slip condition is assumed at the cylinder walls.
- (3) The boundaries of the computational domain are treated as [34,35] ( $\mathbf{U} = ue_1 + ve_2$  and  $\mathbf{X} = xe_1 + ye_2$ )

(a) At the right boundary line

$$\begin{aligned} \frac{\partial u}{\partial x} &= 0, \quad v = 0 \\ \text{If } u \leq 0, \quad T &= 0, \quad P = 0 \\ \text{If } u > 0, \quad \frac{\partial T}{\partial x} &= 0, \quad \frac{\partial P}{\partial x} = 0 \end{aligned} \quad (9)$$

(b) At the centerline

$$\frac{\partial u}{\partial x} = \frac{\partial v}{\partial x} = \frac{\partial P}{\partial x} = \frac{\partial T}{\partial x} = 0 \quad (10)$$

(c) At the top boundary line

$$\begin{aligned} u &= 0, \quad \frac{\partial v}{\partial y} = 0 \\ \text{If } v \leq 0, \quad T &= 0, \quad P = 0 \\ \text{If } v > 0, \quad \frac{\partial T}{\partial y} &= 0, \quad \frac{\partial P}{\partial y} = 0 \end{aligned} \quad (11)$$

(d) At the bottom boundary line

$$\begin{aligned} u &= 0, \quad \frac{\partial v}{\partial y} = 0 \\ \text{If } v \geq 0, \quad T &= 0, \quad P = 0 \\ \text{If } v < 0, \quad \frac{\partial T}{\partial y} &= 0, \quad \frac{\partial P}{\partial y} = 0 \end{aligned} \quad (12)$$

(e) At the cylinder surfaces

$$u = 0, \quad v = 0, \quad T = 1 \quad (13)$$

Finally, the local and averaged Nusselt numbers for each elliptical cylinder are defined as ( $n_s$  is the unit outward vector normal to the cylinder surface)

$$\begin{aligned} \text{Nu}_\theta &= \frac{h(2a)}{k} = -\left(\frac{\partial T}{\partial n_s}\right) \\ \overline{\text{Nu}}_i &= \frac{1}{S} \int_S \text{Nu}_\theta dS \end{aligned} \quad (14)$$

### 3 Results and Discussion

In the present section, the present numerical approach was first validated against the experimental data and the previously published numerical solutions for Newtonian and power-law fluids. Subsequently, it was followed by a detailed numerical mesh size study to ensure mesh-independent numerical solutions. Finally, new numerical results were presented on the natural convection of power-law fluids from an array of elliptical isothermal tubes. The specification of all presented numerical cases in this work is summarized in Table 1.

**3.1 Validation of the Numerical Method.** Figure 3 shows the comparison between the present numerical results and the experimental data of Yousefi and Ashjaee [5] for a Newtonian fluid ( $n=1$ ) around a single ellipse at  $\text{Pr}=0.7$  and  $\text{Ra}=1000$ . Figures 3(a) and 3(b) present the results for  $E=0.67$  and  $E=1.25$ , respectively. The comparison clearly shows a good agreement between the present results and the experimental data. The maximum deviation between the numerical results and the experimental data is less than 5%. For the case of  $E=0.67$ , the local Nusselt number decreases along the azimuth angle, but the local Nusselt number exhibits local maxima for the case  $E=1.25$ , which are well-predicted by the present numerical code.

A comparison is also made with the numerical results of Sasmal and Chhabra [31] who simulated the natural convection of a non-Newtonian power-law fluid around a single elliptic cylinder for  $\text{Pr}=10$  and  $\text{Gr}=1000$  (Figs. 4(a) and 4(b)). Again, the present numerical results show a good agreement with the previous data of Sasmal and Chhabra [31], which further corroborates the accuracy and reliability of our numerical simulations. The final

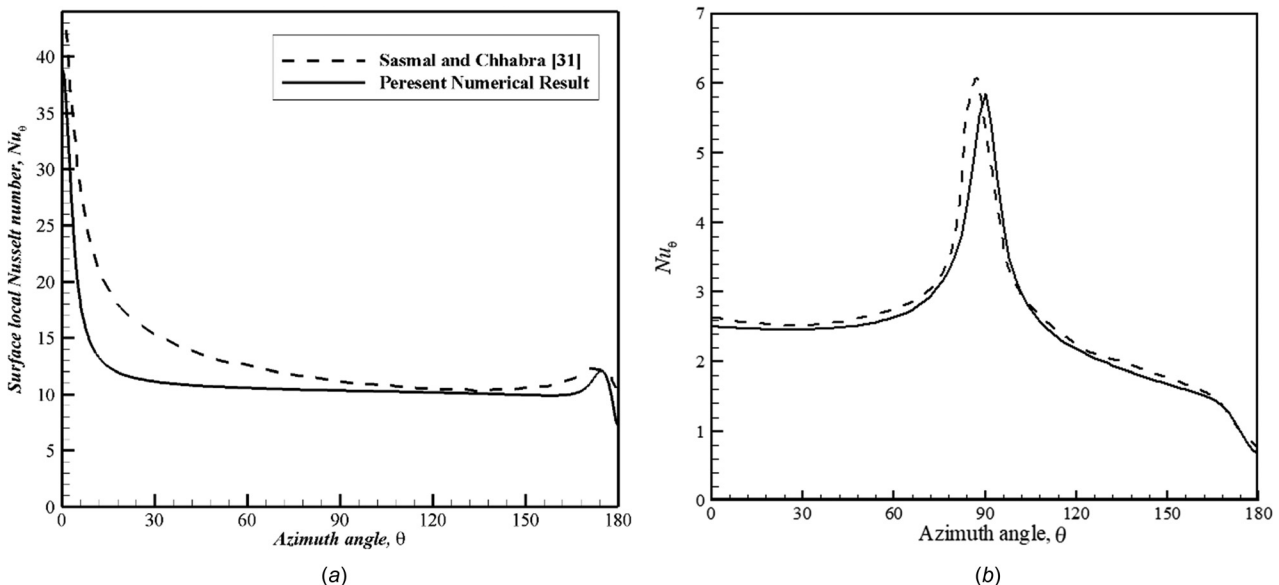
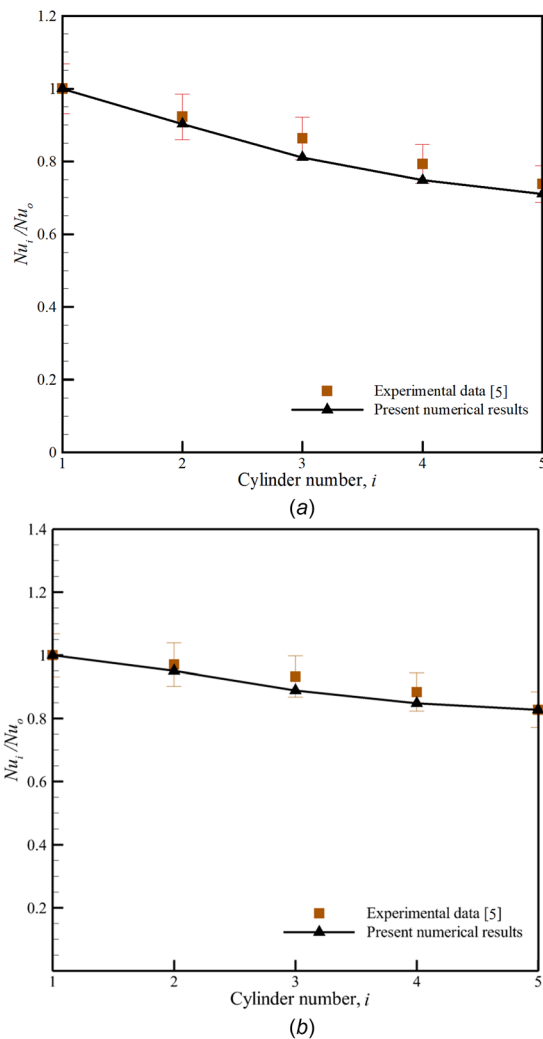


Fig. 4 Comparison between the present numerical results and the numerical results of Sasmal and Chhabra [31] for non-Newtonian fluids around a single ellipse at  $\text{Pr}=10$  and  $\text{Gr}=1000$ : (a)  $n=0.3$  and  $E=0.2$  and (b)  $n=1.0$  and  $E=5$



**Fig. 5 Comparison between the present numerical results and the experimental data of Yusefi and Ashjaee [5] for a Newtonian fluid around an elliptic tube bundle at  $\text{Pr} = 0.7$  and  $E = 0.67$ : (a)  $\text{Ra} = 1000$  and (b)  $\text{Ra} = 2000$**

validation case is the experimental work of Yousefi and Ashjaee [5] on a tube bundle with five elliptic cylinders submerged in a Newtonian fluid. As can be seen in Figs. 5(a) and 5(b), the present numerical results are in good agreement with the available experimental data. The maximum deviation between the numerical results and the experimental data is less than 6.02%.

**3.2 Mesh Size Study.** In this study, a structured quadrilateral grid is used for the simulations as depicted in Fig. 1. The numerical mesh is clustered near the cylinder surfaces to increase the resolution of temperature field in this area where natural convection heat transfer occurs. In Table 2, the effect of mesh size is

**Table 3 The effect of domain size on the array average Nusselt number ( $\text{Pr} = 0.7$ ,  $\text{Ra} = 2000$ ,  $n = 1.0$ , and  $E = 0.67$ )**

The domain size ( $L/a$ )	Array average Nusselt number ( $\overline{\text{Nu}}_a$ )
80	3.227
160	3.227
240	3.224
320	3.223

presented on the average Nusselt numbers on the cylinder surfaces ( $\overline{\text{Nu}}_i$  is the average Nusselt number of  $i$ th cylinder and  $\overline{\text{Nu}}_o$  is the average Nusselt number for a single elliptic cylinder under identical thermal conditions). As can be seen, using a numerical mesh with 77,200 cells can produce a mesh-independent numerical result. Therefore, this mesh is used throughout this study. As a final note in this section, the effect of the computational domain size ( $L$ ) on the array average Nusselt number ( $\overline{\text{Nu}}_a$ ), as defined in Eq. (15), is investigated in Table 3. As can be seen, the effect of domain size on the numerical solutions is negligible for  $L/a > 80$ . As a result, we used this domain size throughout this study

$$\overline{\text{Nu}}_a = \frac{1}{N} \sum_{i=1}^N \overline{\text{Nu}}_i; \quad N = 5 \quad (15)$$

Based on the presented validations and mesh size study, it can be confirmed that the current numerical code is able to predict the natural convection phenomenon of both Newtonian and non-Newtonian fluids within a bundle of elliptic tubes. Therefore, in the subsequent sections, we present our new numerical results concerning the natural convection heat transfer within a vertical array of elliptic cylinders submerged into a stagnant pool of inelastic non-Newtonian fluids.

**3.3 Heat Transfer Rate.** Figure 6 shows the variations of the local Nusselt number with the azimuth angle for  $\text{Pr} = 10$ ,  $\text{Gr} = 2000$ , and  $S/2a = 2$  for two aspect ratios  $E = 2.5$  and  $E = 0.4$  of elliptical tubes. As can be seen, the shape of the local Nusselt number profile strongly depends on the aspect ratio of the tube and also on the rheological behavior of the non-Newtonian working fluid. For  $E = 0.4$  ( $E < 1$ , a so-called slender configuration), the trend of local Nusselt number is always decreasing as the azimuth angle increases except for the case of shear thinning fluid ( $n = 0.2$ ) where a local maximum is detectable in the Nusselt profile around  $\theta = 12$  deg. Moreover, for the case  $E = 2.5$  ( $E > 1$ , so-called blunt configuration), a notable local maximum appears in the local Nusselt number profile around  $\theta = 90$  deg for all cylinders for both shear thinning and shear thickening fluids; however, for the shear thinning fluid, another local maximum emerged around  $\theta = 36$  deg.

To justify the trends as mentioned earlier in the variations of local Nusselt number on solid surfaces, in Fig. 7, the contours of apparent viscosity, and in Fig. 8, the variation of fluid viscosity on solid surfaces are depicted for various cases, and in this figure, lighter areas correspond to the lower viscosity levels. For the case

**Table 2 The effect of mesh size on the average Nusselt number ( $\text{Pr} = 0.7$ ,  $\text{Ra} = 2000$ ,  $n = 1.0$ , and  $E = 0.67$ )**

Maximum error with respect to the experimental data of Yusefi and Ashjaee [5] (%)	$\frac{y}{H}$					Mesh size
	1	0.75	0.5	0.25	0	
9.15	0.702	0.723	0.784	0.887	1	19,300
6.25	0.705	0.735	0.809	0.892	1	35,200
6.02	0.71	0.748	0.811	0.903	1	77,200

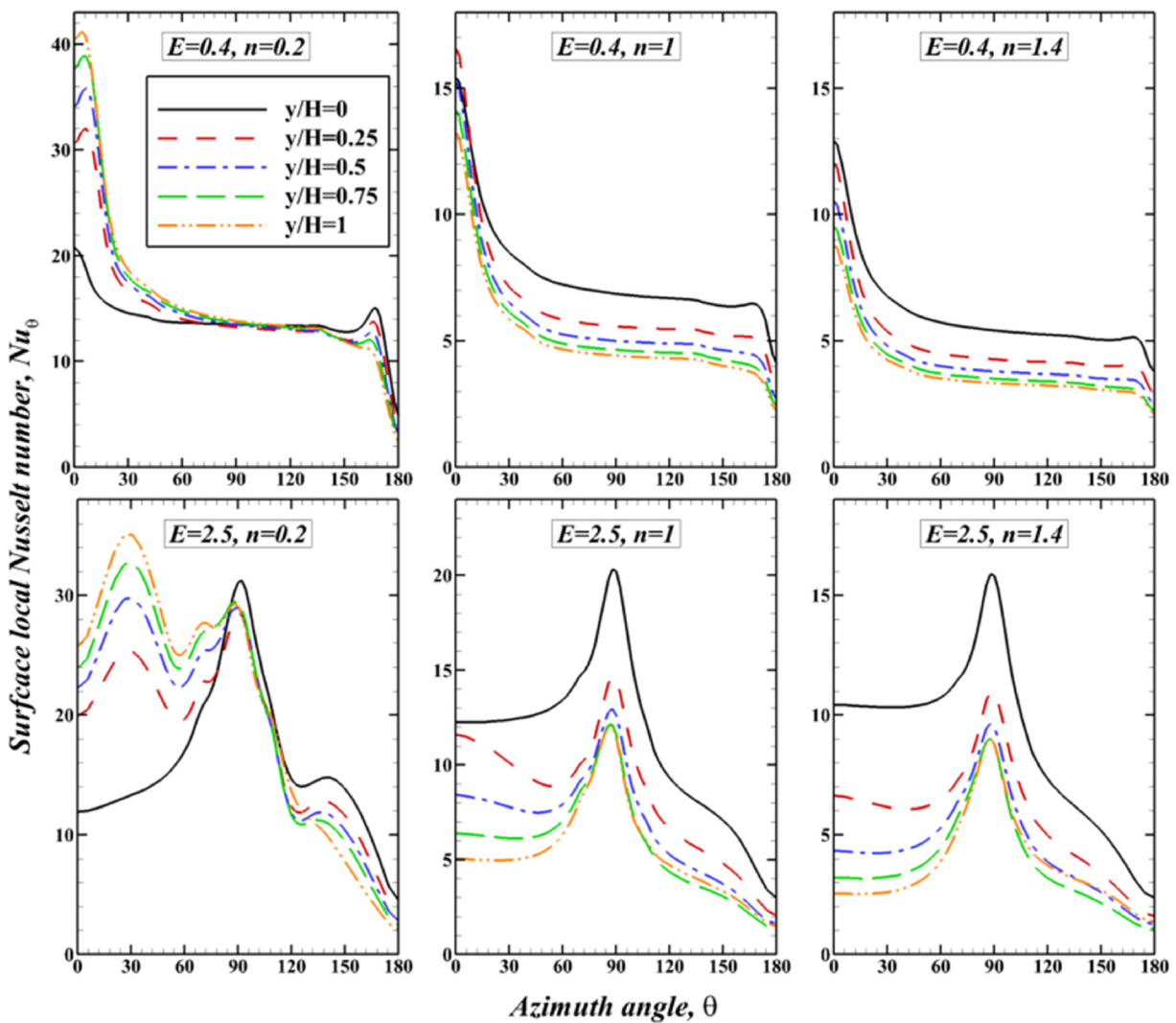


Fig. 6 Variations of the local Nusselt number with azimuth angle for  $\text{Pr} = 10$ ,  $\text{Gr} = 2000$ , and  $S/2a = 2$

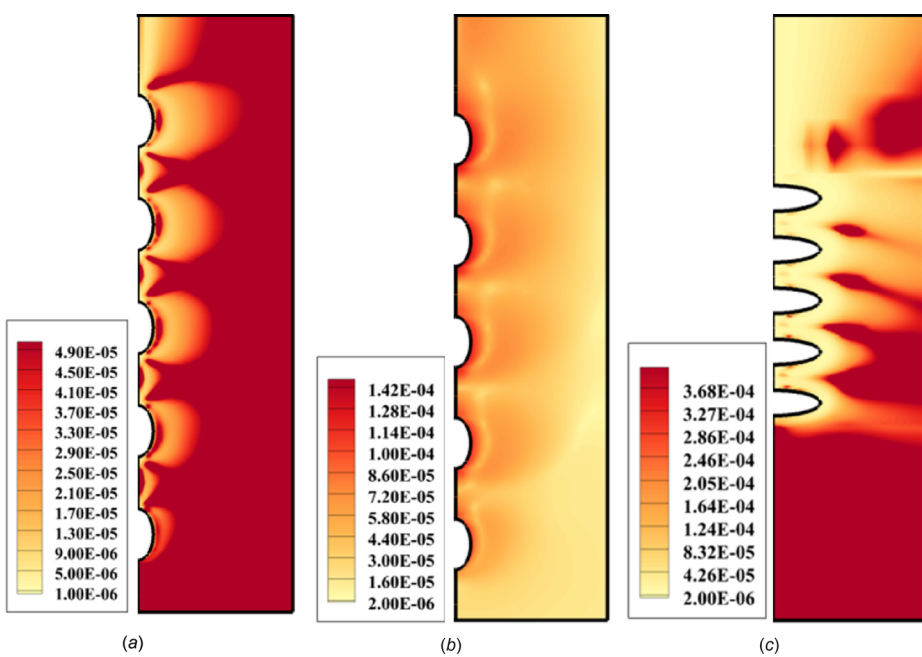
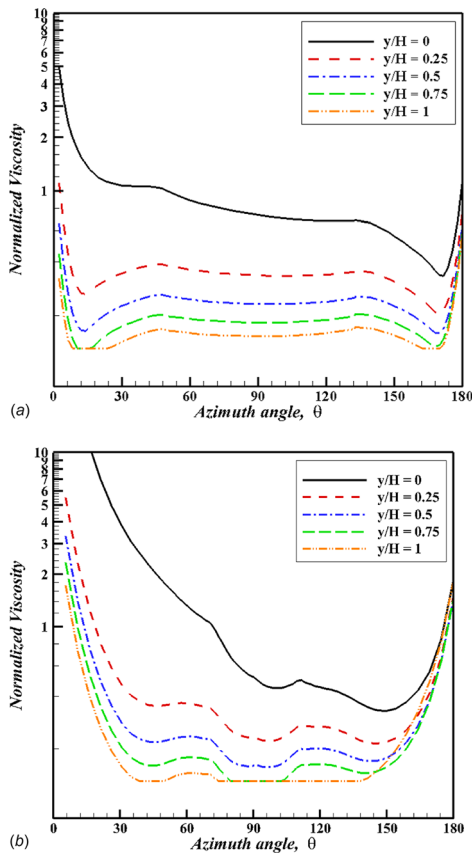


Fig. 7 Apparent viscosity contours at  $\text{Pr} = 10$ ,  $\text{Gr} = 2000$ , and  $S/2a = 2$ : (a)  $E = 0.4$  and  $n = 0.2$ , (b)  $E = 0.4$  and  $n = 1.4$ , and (c)  $E = 2.5$  and  $n = 0.2$



**Fig. 8 Variations of apparent fluid viscosity on the surface of elliptic cylinders for (a)  $E=0.4$  and (b)  $E=2.5$  ( $n=0.2$ ,  $Pr=10$ ,  $Gr=2000$ , and  $S/2a=3$ )**

of  $E=0.4$ , the development of thermal and hydrodynamic boundary layers with azimuth angle tends to decrease the temperature gradient on the cylinder surfaces and subsequently reduce the local Nusselt number. On the other hand, the variation of power-law fluid viscosity prompted by bouncy-induced shear flow influences the overall strength of natural fluid flow and heat transfer rate. For the case of shear thinning fluid with power-law index ( $n=0.2$ ), the reduction of apparent fluid viscosity near the frontal stagnation point is extremely fierce due to high shear rates in that area (see Figs. 7(a)–7(c)). This intense shear flow can be attributed to the collision between upcoming plume from lower cylinders and the free convection boundary layer formed around each cylinder due to thermally induced density variation, therefore, it compensates the decreasing effect of the boundary layer development on the heat transfer rate, and as a result, the local Nusselt number increases to reach a local maxima around  $\theta=12$  deg where the apparent viscosity is minimum (see Figs. 8(a) and 8(b)). The only exception is the first cylinder for which the buoyancy induced flow is weaker in comparison to the upper cylinders, and as a result, a decreasing function is observed for the apparent viscosity, and subsequently, no maximum point appears in the local variations of the Nusselt number.

The local maximum point is more notable for the upper elliptic cylinders ( $y/H > 0.25$ ) where the plumes from lower cylinders promote the shear flow around the upper cylinders and also reduce the apparent viscosity of the fluid as depicted in Fig. 7. For higher azimuth angles, the thickening of the thermal boundary layer prevails, which results in a steep reduction of local Nusselt number. In contrast to the case of shear thinning fluid, for the shear thickening fluid ( $n=1.4$ ), the two aforementioned effects (viscosity increase and boundary layer growth) decrease the temperature gradient and reduce the intensity of natural fluid flow, and as a result, a monotonically decreasing local Nusselt number profile is obtained for all cylinders.

For the case  $E=2.5$ , the appearance of the local maximum around  $\theta=90$  deg in the local Nusselt number profile is due to the

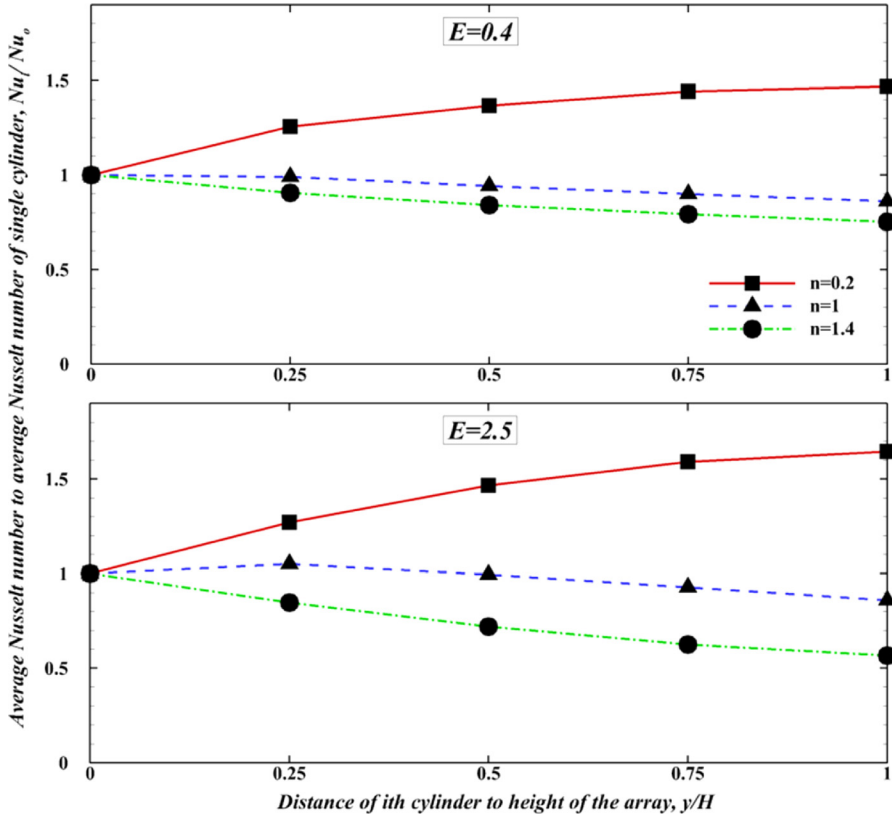


**Fig. 9 Variations of  $(Nu_i/Nu_o)$  along the height of the tube array for  $Pr=10$ ,  $Gr=2000$ , and  $S/2a=3$**

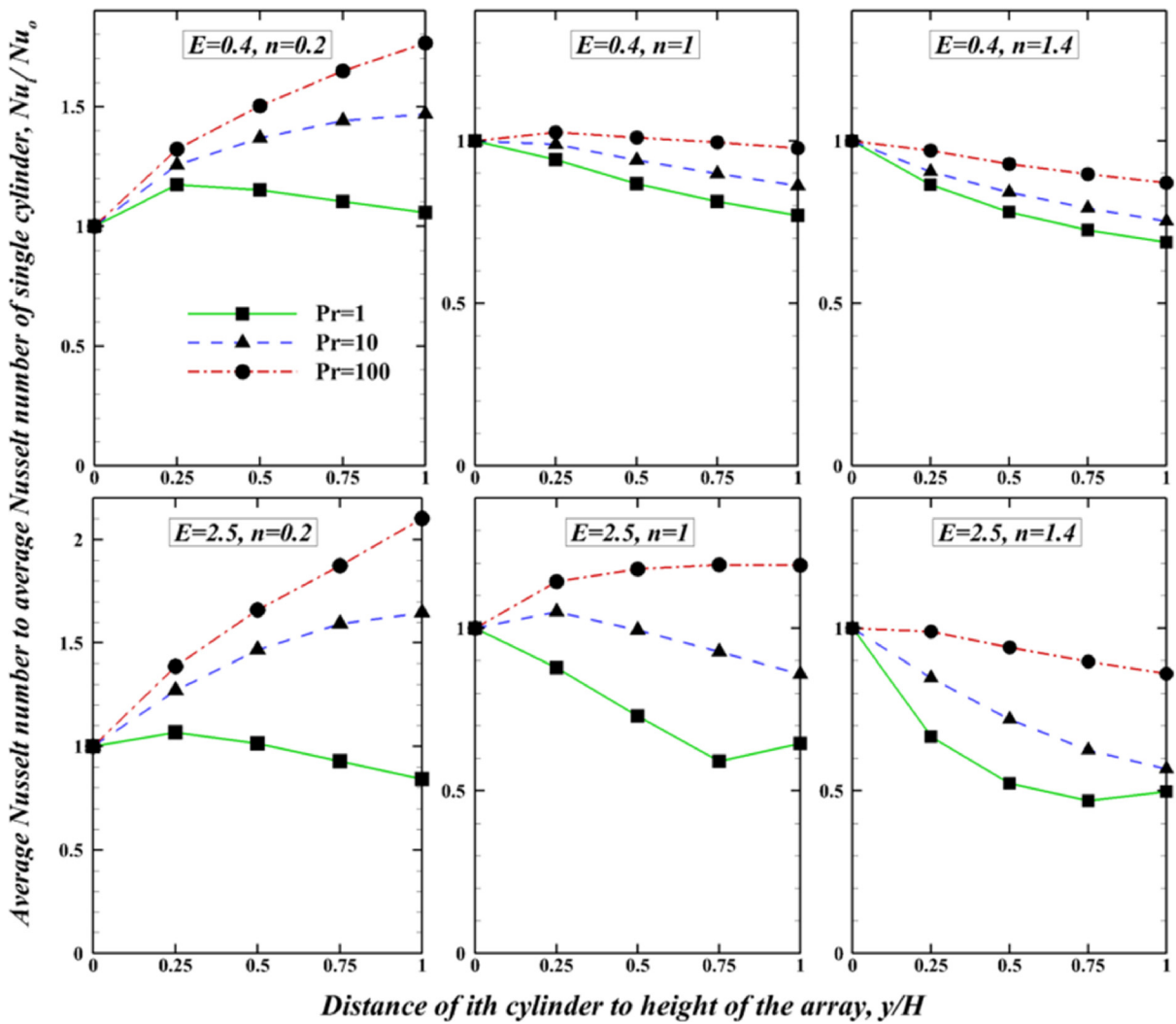


Fig. 10 Variations of ( $\bar{N}_{u_i}/\bar{N}_{u_o}$ ) along the height of the tube array for  $Gr = 2000$  and  $S/2a = 3$

obstructing effect of cylindrical surfaces which suppresses the natural fluid flow for  $\theta < 90$  deg. Moreover, for the highly shear thinning fluid, a second maximum emerges around  $\theta = 36$  deg due to intense viscosity reduction prompted by the shear flow as shown in Fig. 8 (the first two minimum points in the apparent viscosity profiles). Additionally, this second maxima intensify along the vertical coordinate where the higher velocity gradients and the lower viscosity levels exist as shown in Fig. 7. However, for the first cylinder, the flow field is in initial stages of development, and a single maximum is observed in the Nusselt number profile even for this highly shear thinning fluid. This behavior can be justified by noting the variations of apparent viscosity on the surface of the first cylinder in Fig. 8 where no initial minimum is seen for  $\theta < 90$  deg.

In Figs. 9 and 10, the ratio of average Nusselt number on each elliptical tube of the array to the corresponding Nusselt number for a single tube ( $\bar{N}_{u_i}/\bar{N}_{u_o}$ ) is illustrated. As can be seen in Fig. 9, for both slender and blunt configurations of the tube array, the heat transfer rate from the first tube on the array is identical to the corresponding heat transfer rate from a single elliptical tube. However, due to the so-called bundle effect, the value of heat transfer rates from upper tubes in the array differs from a single tube, and depending on the value of the aspect ratio, the Prandtl number, and the power-law index, it could be larger or smaller

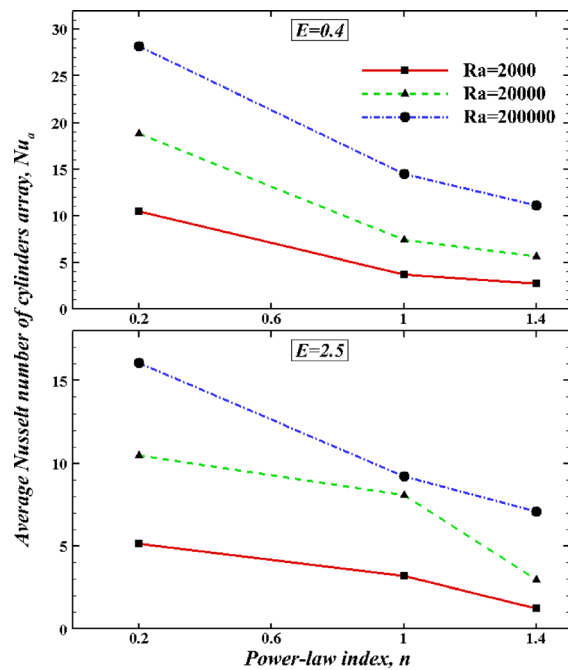


Fig. 11 The effect of the power-law index on the average Nusselt number for the tube at  $S/2a = 3$  and  $Pr = 10$

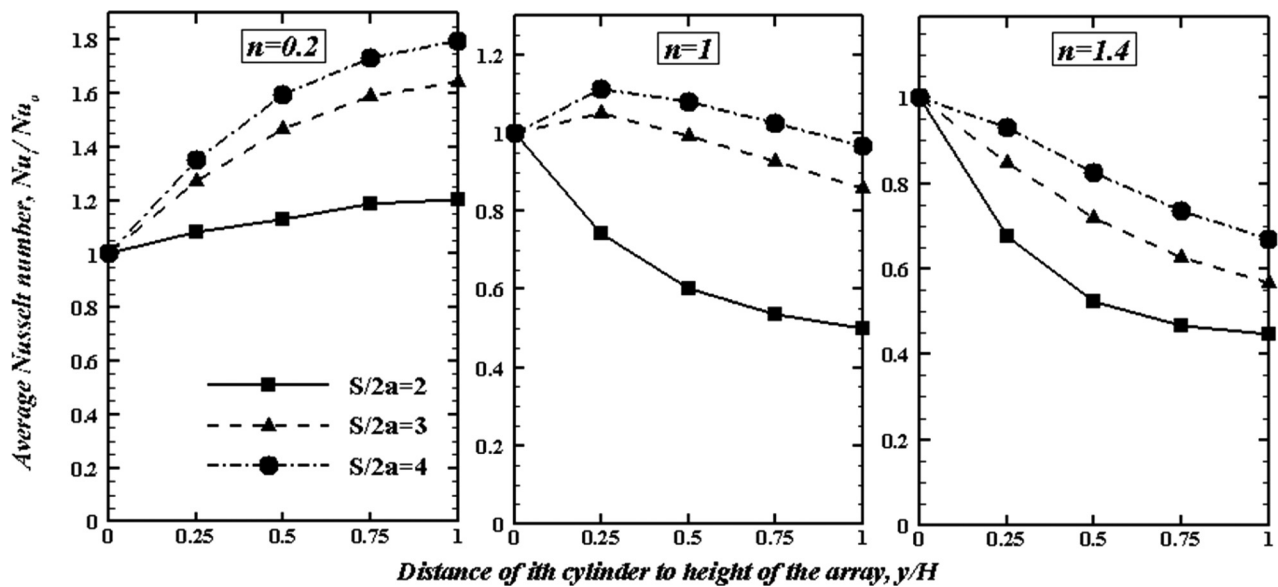


Fig. 12 The effect of center to center distance on  $(\overline{Nu}_i/\overline{Nu}_o)$  for  $\text{Pr} = 10$ ,  $\text{Gr} = 2000$ , and  $E = 0.4$

than the heat transfer rate from a single tube under identical thermal conditions.

To study the bundle effect, it should be noted that the value of the average Nusselt number for each elliptical tube within the tube bundle (which could be used to compare the thermal performance of upper tubes in the tube array with the thermal performance of a single tube) is strongly affected by the upward flow of the hot fluid which passes the lower tubes and arrives at the surfaces of upper tubes (the so-called plume). This plume has three competing effects. First, it increases the fluid velocity around the upper tube in comparison to a single elliptic tube under the similar thermal condition and promotes the convective motion and heat transfer of power-law fluid around the cylinders. Second, this intensified shear flow triggers more drastic viscosity variations around the upper tubes, and for the case of a shear thinning fluid, results in the decrease in fluid viscosity along the vertical coordinate, however, the reverse trend is observed for a shear thickening fluid. Finally, the arrival of hot fluid at the surface of the upper tube reduces the temperature gradient and has an adverse effect on the heat transfer rate. Thus, the superposition of these three effects determines the variation of the Nusselt number within the tube bundle.

As can be seen in Fig. 10, the effect of viscosity (or equivalently momentum diffusion) is less significant when the Prandtl number is relatively low (i.e.,  $\text{Pr} = 1$ ), and an almost decreasing trend for the Nusselt number is observed moving upward within the tube array. This observation means that the thermal performances of elliptical tubes within a vertical array are worse than a single tube under similar thermal conditions when the Prandtl number is low. Moreover, for the shear thickening fluid, this decreasing trend is also obtained for higher Prandtl numbers because of viscosity increase as it flows upward in the bundle. In contrast, for the shear thinning fluid and for high Prandtl numbers, the effect of viscosity reduction becomes dominant, and the Nusselt number increases from the bottom tube to the top one. This phenomenon is more pronounced for blunt configuration because of the larger area on the top of each tube, which is affected by the bottom ones. In this case, when the fluid exhibits shear-thinning rheological behavior and the corresponding Prandtl number is large enough, the use of a tube array is profitable in comparison to the single tube because the heat transfer rate from upper cylinders is larger than the first cylinder which behaves similar to a single cylinder. Additionally, according to the results depicted in Fig. 10, it can be concluded that regardless of the tube orientation

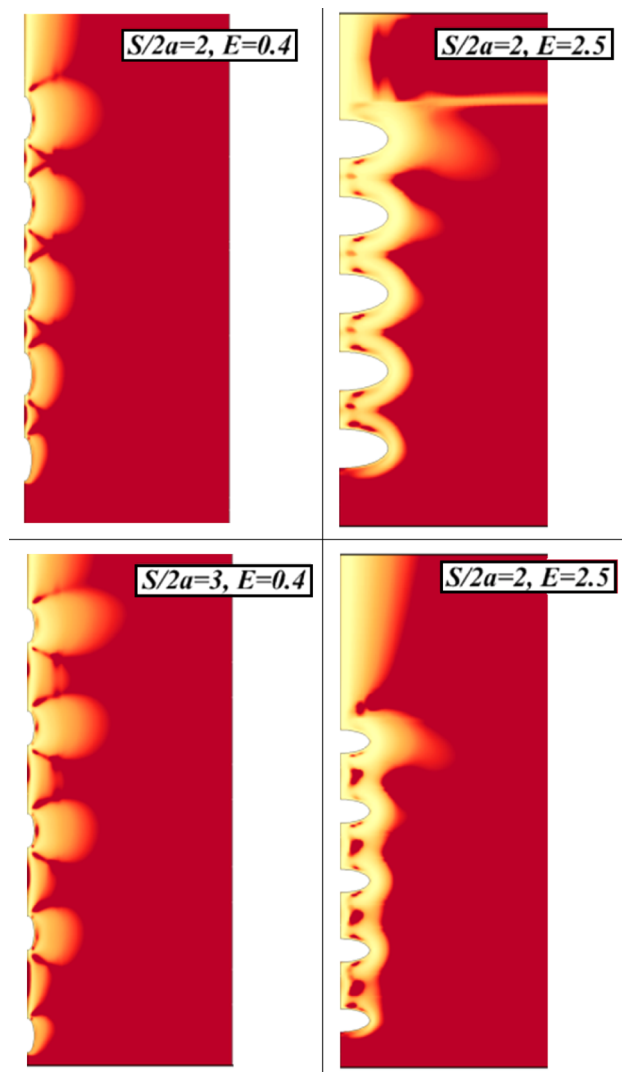
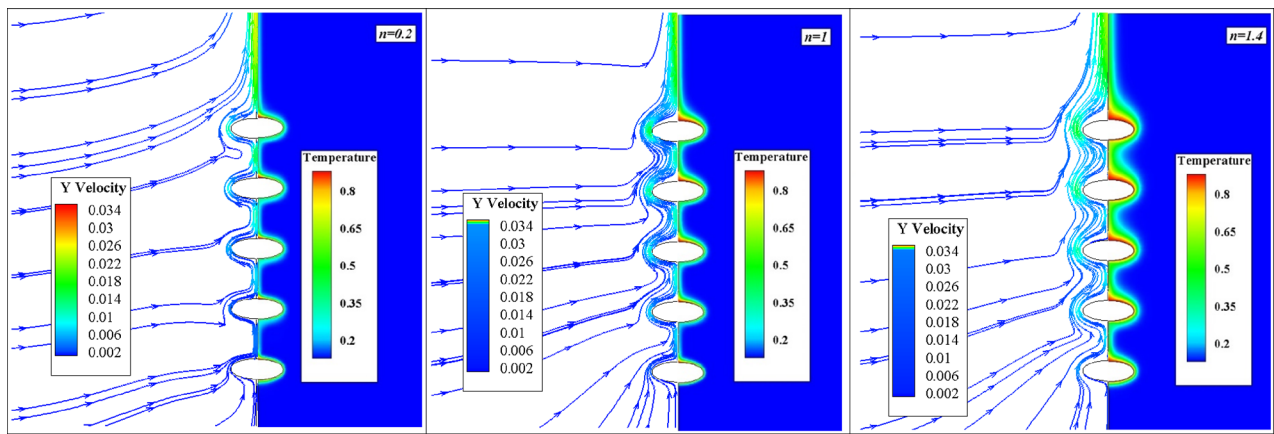
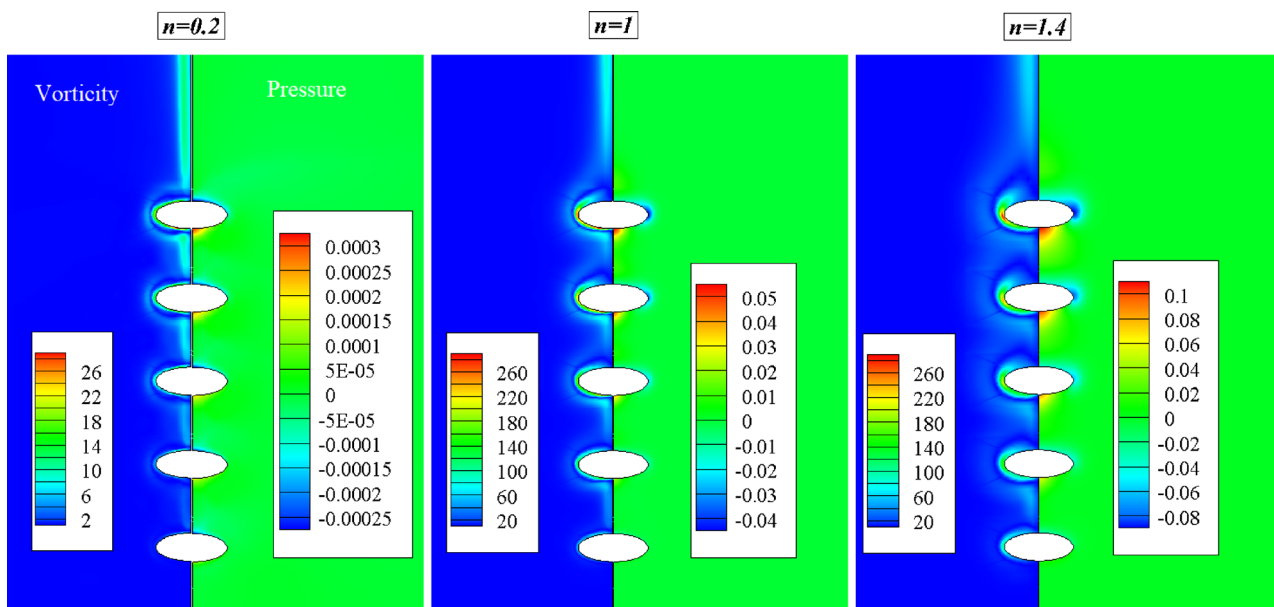


Fig. 13 The effect of center to center distance on viscosity contours for  $\text{Pr} = 10$  and  $\text{Gr} = 2000$  (contour levels from  $10^{-6}$  to  $10^{-4}$ )



**Fig. 14** Distributions of temperature (right) and streamline (left) within the domain for  $\text{Pr} = 10$ ,  $\text{Gr} = 2000$ ,  $E = 2.5$ , and  $S/2a = 3$



**Fig. 15** Distributions of pressure (right) and vorticity (left) within the domain for  $\text{Pr} = 10$ ,  $\text{Gr} = 2000$ ,  $E = 2.5$ , and  $S/2a = 3$

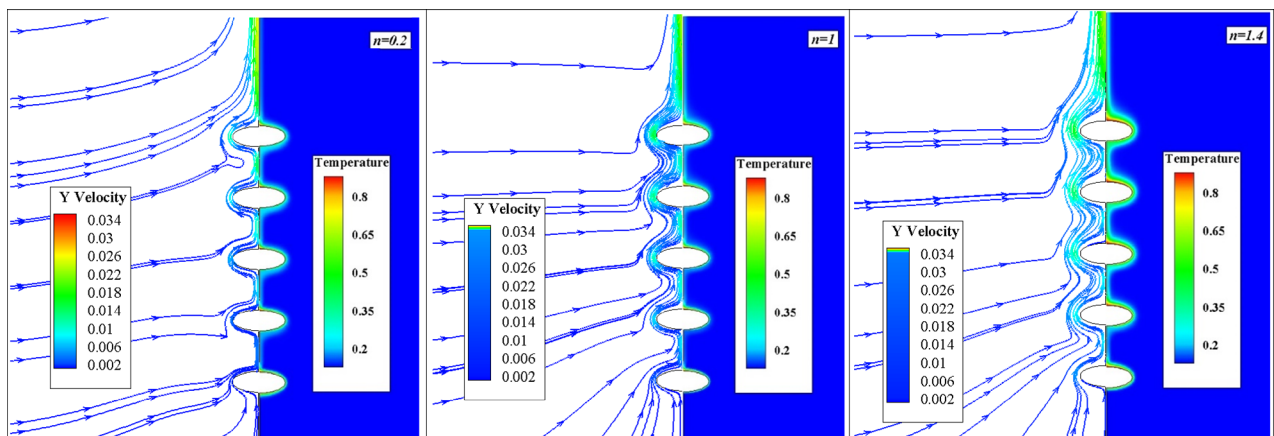


**Fig. 16** Distributions of temperature (right) and streamline (left) within the domain for  $\text{Pr} = 100$ ,  $\text{Gr} = 2000$ ,  $E = 2.5$ , and  $S/2a = 3$

and power-law index, the ratio ( $\overline{\text{Nu}_i}/\overline{\text{Nu}_o}$ ) increases with the increase in the Prandtl number, which can be attributed to the thinning of the thermal boundary layer on the heated surfaces. Furthermore, the changes in the ratio ( $\overline{\text{Nu}_i}/\overline{\text{Nu}_o}$ ) along the vertical coordinate become more considerable when the Prandtl number increases, because the convection effect increases with the increase in the Prandtl number (boundary layers are thinner for higher Pr numbers) which results in the increase in the average Nusselt number from the bottom tube to the top one.

In Fig. 11, the variations of the averaged Nusselt number of the tube array are shown. As can be seen, the tube array average Nusselt number decreases when the power-law index increases, and in contrast, it increases as Ra increases. The first trend can be attributed to the increase in fluid viscosity with the power-law index which weakens the natural convection flow around the elliptic cylinders and the second trend is the result of fluid flow augmentation with increasing Ra (i.e., the deriving temperature difference).

The effect of the pitch to diameter ratio ( $S/2a$ ) on the average Nusselt number within the bundle is depicted in Fig. 12. The presented results are for the condition  $\text{Pr} = 10$ ,  $\text{Gr} = 2000$ , and  $E = 0.4$ . The results show that the increase in  $S/2a$  increases the average Nusselt number along the tube array, because when the pitch to diameter ratio increases the average traveling distance of the plume rising from the lower tube increases until it reaches to the surface of the upper tube. This effect causes the cooling of the plume in the tube spacing and results in the increase in temperature difference at the upper tube, which consequently increases the driving force of natural convection heat transfer. The effect of tube spacing increases as the power-law index deviates further from the Newtonian value of ( $n = 1$ ) into the shear-thinning zone of ( $n < 1$ ) where the more tube spacing means the more distance for the viscosity reduction within the field (see Fig. 13).

**3.4 Flow and Temperature Fields.** The distributions of temperature, vorticity, pressure, and streamline within the computational domain are presented in Figs. 14–16 (these figures show only the central part of the computational domain to provide a better view of velocity and temperature fields in the vicinity of the tube array). The figures clearly show that the cold fluid is entrained toward the hot tubes and then moves upward, which causes a buoyancy-induced flow. The heated fluid departed from the lower tubes arrives at the surface of the upper tube, and as a result, high-pressure zones are recognizable below each one of these upper tubes and the high-pressure zone grows as the fluid flows upward within the bundle. Low-pressure zones also form at the top of second to fifth cylinders due to the upward fluid motion.

Moreover, the size of the abovementioned low/high-pressure zones around solid surfaces increases as the power-law index increases. The vorticity contours presented in Fig. 15 reveal that the shear thinning flow behavior ( $n = 0.2$ ) decreases the magnitude of vorticity in the considered buoyancy-driven flow, and in contrast, notable levels of vorticity magnitude are reported around the elliptical cylinder for a shear-thickening fluid ( $n = 1.4$ ). For both shear thinning and shear thickening flow fields, the location of maximum vorticity magnitude is around  $\theta = 90$  deg; however, for the case of  $n = 0.2$ , a thin high vorticity stream is formed at the top of each tube around  $\theta = 180$  deg as well.

Additionally, a recognizable trend in Fig. 15 is the increase in thermal and hydrodynamics boundary layer thicknesses around all elliptic cylinders with the increase in the power-law index. The thickness increase is almost uniform from the second to the fifth cylinder. Figure 16 shows the similar results for the condition  $\text{Pr} = 100$ ,  $\text{Gr} = 2000$ ,  $E = 2.5$ , and  $S/2a = 3$ . In this case, the streamlines are more deviated, and the boundary layers are considerably thinner compared to the case  $\text{Pr} = 10$  (Figs. 14 and 15), which implies the more convection effect, and consequently, the

higher heat transfer rate. Finally, for this blunt configuration, the compactness of streamlines around the point ( $\theta = 90$  deg) is a striking feature which influences the temperature field and heat transfer rate as it was discussed earlier.

## 4 Conclusion

In this work, the natural convection phenomenon of non-Newtonian fluids within an elliptic tube bundle was studied numerically. The effects of different pertinent parameters such as Grashof number, Prandtl number, tube to tube spacing (bundle effect), power-law index, and ellipse orientation on the flow pattern and heat transfer coefficient within an elliptic tube bundle were thoroughly investigated. It was found that for a highly shear thinning liquid, a local maximum appeared in the local Nusselt number profile near the frontal stagnation point. This phenomenon was attributed to the shear-induced reduction of fluid viscosity, which promotes the natural convection heat transfer rate. This local maximum became more significant for upper cylinders in the tube array. The only exception was the first tube in the bundle for which the natural fluid circulation was not strong enough to produce such local maximum in Nusselt number profile around frontal stagnation point. The results also showed that the appearance of the new local maximum of the Nusselt number was independent of the tube orientation. However, for the blunt configuration, the maximum point was shifted toward the downstream due to partial blockage of flow domain by the horizontal elliptic cylinder, and this blocking effect produced a second maximum in Nusselt number profile around the point ( $\theta = 90$  deg) in contrast to the case of a slender configuration. Furthermore, for a shear thickening fluid and in a slender configuration, the local Nusselt number exhibited a decreasing trend for all the tubes, but for the blunt configuration, only one maximum point was obtained for the local Nusselt number around  $\theta = 90$  deg.

## Nomenclature

$a$	= elliptic cylinder semi-axis along the flow direction (m)
$b$	= elliptic cylinder semi-axis normal to the flow direction (m)
$C$	= specific heat capacity (J kg/K)
$e$	= rate of deformation tensor (1/s)
$E$	= aspect ratio
$g$	= gravitational acceleration (m/s <sup>2</sup> )
$\text{Gr}$	= Grashof number
$I_2$	= second invariant of the rate of the strain tensor
$k$	= thermal conductivity (W/m K)
$m$	= power-law consistency index (Pa·s <sup>n</sup> )
$n$	= power-law index
$\text{Nu}$	= Nusselt number
$P$	= pressure
$\text{Pr}$	= Prandtl number
$\text{Ra}$	= Rayleigh number
$T$	= temperature
$T_s$	= cylinder surface temperature (K)
$T_\infty$	= quiescent fluid temperature (K)
$\Delta T$	= temperature difference (K)
$u$	= $x$ -component of velocity
$v$	= $y$ -component of velocity
$x, y$	= Cartesian co-ordinates

## Greek Symbols

$\beta$	= coefficient of volume expansion (1/K)
$\eta$	= viscosity (Pa·s)
$\rho$	= density (kg/m <sup>3</sup> )
$\tau$	= stress tensor

## Subscripts

$o$	= bottom cylinder
$s$	= cylinder wall

$i$  = cylinder number  
 $\infty$  = ambient condition

## References

- [1] Ilyas, S. U., Pendyala, R., and Narahari, M., 2017, "An Experimental Study on the Natural Convection Heat Transfer in Rectangular Enclosure Using Functionalized Alumina-Thermal Oil-Based Nanofluids," *Appl. Therm. Eng.*, **127**, pp. 765–775.
- [2] He, Z., Fang, X., Zhang, Z., and Gao, X., 2016, "Numerical Investigation on Performance Comparison of Non-Newtonian Fluid Flow in Vertical Heat Exchangers Combined Helical Baffle With Elliptic and Circular Tubes," *Appl. Therm. Eng.*, **100**, pp. 84–97.
- [3] Cho, C.-C., Chen, C.-L., Hwang, J.-J., and Chen, C. O-K., 2013, "Natural Convection Heat Transfer Performance of Non-Newtonian Power-Law Fluids Enclosed in Cavity With Complex-Wavy Surfaces," *ASME J. Heat Transfer*, **136**(1), p. 014502.
- [4] Noori Rahim Abadi, S. M. A., and Jafari, A., 2012, "Investigating the Natural Convection Heat Transfer From Two Elliptic Cylinders in a Closed Cavity at Different Cylinder Spacings," *Heat Transfer Res.*, **43**, pp. 259–284.
- [5] Yousefi, T., and Ashjaee, M., 2007, "Experimental Study of Natural Convection Heat Transfer From Vertical Array of Isothermal Horizontal Elliptic Cylinders," *Exp. Therm. Fluid Sci.*, **32**(1), pp. 240–248.
- [6] Yousefi, T., Paknezhad, M., Ashjaee, M., and Yazdani, S., 2009, "Effects of Confining Walls on Heat Transfer From a Vertical Array of Isothermal Horizontal Elliptic Cylinders," *Exp. Therm. Fluid Sci.*, **33**(6), pp. 983–990.
- [7] Guha, A., and Pradhan, K., 2014, "Natural Convection of Non-Newtonian Power-Law Fluids on a Horizontal Plate," *Int. J. Heat Mass Transfer*, **70**, pp. 930–938.
- [8] Mulamootil, J. K., and Dash, S. K., 2017, "Numerical Investigation of Natural Convection Heat Transfer From an Array of Horizontal Fins in Non-Newtonian Power-Law Fluids," *ASME J. Heat Transfer*, **140**(2), p. 022501.
- [9] Sairamu, M., and Chhabra, R. P., 2013, "Natural Convection in Power-Law Fluids From a Tilted Square in an Enclosure," *Int. J. Heat Mass Transfer*, **56**(1–2), pp. 319–339.
- [10] Gangawane, K. M., and Manikandan, B., 2017, "Laminar Natural Convection Characteristics in an Enclosure With Heated Hexagonal Block for Non-Newtonian Power Law Fluids," *Chin. J. Chem. Eng.*, **25**(5), pp. 555–571.
- [11] Turan, O., Lai, J., Poole, R. J., and Chakraborty, N., 2013, "Laminar Natural Convection of Power-Law Fluids in a Square Enclosure Submitted From Below to a Uniform Heat Flux Density," *J. Non-Newtonian Fluid Mech.*, **199**, pp. 80–95.
- [12] Darbouli, M., Métivier, C., Leclerc, S., Nouar, C., Bouteera, M., and Stemmelen, D., 2016, "Natural Convection in Shear-Thinning Fluids: Experimental Investigations by MRI," *Int. J. Heat Mass Transfer*, **95**, pp. 742–754.
- [13] Abou-Ziyah, H., Kalender, A., Shedad, M., and Abdel-Hameed, H., 2017, "Experimental Investigation of Free Convection From Short Horizontal Cylinder to Newtonian and Power-Law Liquids of Large Prandtl Numbers," *Exp. Therm. Fluid Sci.*, **86**, pp. 102–116.
- [14] Moradi, H., Bazooyar, B., Etemad, S. G., and Moheb, A., 2015, "Influence of the Geometry of Cylindrical Enclosure on Natural Convection Heat Transfer of Newtonian Nanofluids," *Chem. Eng. Res. Des.*, **94**, pp. 673–680.
- [15] Lemus-Mondaca, R. A., Moraga, N. O., and Riquelme, J., 2013, "Unsteady 2D Conjugate Natural Non-Newtonian Convection With Non-Newtonian Liquid Sterilization in Square Cavity," *Int. J. Heat Mass Transfer*, **61**, pp. 73–81.
- [16] Alsabery, A. I., Chamkha, A. J., Saleh, H., and Hashim, I., 2017, "Transient Natural Convective Heat Transfer in a Trapezoidal Cavity Filled With Non-Newtonian Nanofluid With Sinusoidal Boundary Conditions on Both Sidewalls," *Powder Technol.*, **308**, pp. 214–234.
- [17] Moraga, N. O., Parada, G. P., and Vasco, D. A., 2016, "Power Law Non-Newtonian Fluid Unsteady Conjugate Three Dimensional Natural Convection Inside a Vessel Driven by Surrounding Air Thermal Convection in a Cavity," *Int. J. Therm. Sci.*, **107**, pp. 247–258.
- [18] Matin, M. H., Pop, I., and Khanchezar, S., 2013, "Natural Convection of Power-Law Fluid Between Two-Square Eccentric Duct Annuli," *J. Non-Newtonian Fluid Mech.*, **197**, pp. 11–23.
- [19] Alloui, Z., and Vasseur, P., 2015, "Natural Convection of Carreau–Yasuda Non-Newtonian Fluids in a Vertical Cavity Heated From the Sides," *Int. J. Heat Mass Transfer*, **84**, pp. 912–924.
- [20] Yigit, S., Chen, S., Quinn, P., and Chakraborty, N., 2016, "Numerical Investigation of Laminar Rayleigh–Benard Convection of Bingham Fluids in Square Cross-Sectioned Cylindrical Enclosures," *Int. J. Therm. Sci.*, **110**, pp. 356–368.
- [21] Kefayati, G. R., 2014, "Simulation of Non-Newtonian Molten Polymer on Natural Convection in a Sinusoidal Heated Cavity Using FDLBM," *J. Mol. Liq.*, **195**, pp. 165–174.
- [22] Kefayati, G. R., 2014, "Simulation of Magnetic Field Effect on Natural Convection of Non-Newtonian Power-Law Fluids in a Sinusoidal Heated Cavity Using FDLBM," *Int. Commun. Heat Mass Transfer*, **53**, pp. 139–153.
- [23] Kefayati, G. R., 2014, "FDLBM Simulation of Magnetic Field Effect on Natural Convection of Non-Newtonian Power-Law Fluids in a Linearly Heated Cavity," *Powder Technol.*, **256**, pp. 87–99.
- [24] Chouikh, R., Guizani, A., Maalej, M., and Belghith, A., 1998, "Numerical Study of the Laminar Natural Convection Flow Around Horizontal Isothermal Cylinder," *Renewable Energy*, **13**(1), pp. 77–88.
- [25] Farouk, B., and Gücüeri, S. I., 1981, "Natural Convection From a Horizontal Cylinder-Laminar Regime," *ASME J. Heat Transfer*, **103**(3), pp. 522–527.
- [26] Khoezeymehnezhad, H., and Mirbozorgi, S. A., 2012, "Comparison of Natural Convection Around a Circular Cylinder With a Square Cylinder Inside a Square Enclosure," *J. Mech. Eng. Autom.*, **2**(6), pp. 176–183.
- [27] Badr, H. M., 1997, "Laminar Natural Convection From an Elliptic Tube With Different Orientations," *ASME J. Heat Transfer*, **119**(4), pp. 709–718.
- [28] Shyam, R., Sairamu, M., Nirmalkar, N., and Chhabra, R. P., 2013, "Free Convection From a Heated Circular Cylinder in Confined Power-Law Fluids," *Int. J. Therm. Sci.*, **74**, pp. 156–173.
- [29] Tiwari, A. K., and Chhabra, R. P., 2013, "Laminar Natural Convection in Power-Law Liquids From a Heated Semi-Circular Cylinder With Its Flat Side Oriented Downward," *Int. J. Heat Mass Transfer*, **58**(1–2), pp. 553–567.
- [30] Reymond, O., Murray, D. B., and O'Donovan, T. S., 2008, "Natural Convection Heat Transfer From Two Horizontal Cylinders," *Exp. Therm. Fluid Sci.*, **32**(8), pp. 1702–1709.
- [31] Sasnal, C., and Chhabra, R. P., 2012, "Effect of Aspect Ratio on Natural Convection in Power-Law Liquids From a Heated Horizontal Elliptic Cylinder," *Int. J. Heat Mass Transfer*, **55**(17–18), pp. 4886–4899.
- [32] Sasnal, C., and Chhabra, R. P., 2011, "Laminar Natural Convection From a Heated Square Cylinder Immersed in Power-Law Liquids," *J. Non-Newtonian Fluid Mech.*, **166**(14–15), pp. 811–830.
- [33] Versteeg, H. K., 1995, *An Introduction to Computational Fluid Dynamics: The Finite Volume Approach*, Longman Scientific and Technical, Harlow, UK.
- [34] Shokouhmand, H., and Noori Rahim Abadi, S. M. A., 2010, "Finite Element Analysis of Natural Heat Transfer From an Isothermal Array of Cylinders in Presence of Vertical Oscillations," *Heat Mass Transfer*, **46**(8–9), pp. 891–902.
- [35] Shokouhmand, H., Noori Rahim Abadi, S. M. A., and Jafari, A., 2011, "The Effect of the Horizontal Vibrations on Natural Heat Transfer From an Isothermal Array of Cylinders," *Int. J. Mech. Mater. Des.*, **7**(4), pp. 313–326.